LETTER

doi:10.1038/nature09720

Two-dimensional electron gas with universal subbands at the surface of $SrTiO_3$

A. F. Santander-Syro[1,2], O. Copie[3,4,5], T. Kondo[6], F. Fortuna[1], S. Pailhès[7], R. Weht[8,9], X. G. Qiu[10], F. Bertran[11], A. Nicolaou[11], A. Taleb-Ibrahimi[11], P. Le Fèvre[11], G. Herranz[12], M. Bibes[3,4], N. Reyren[3,4], Y. Apertet[13], P. Lecoeur[13], A. Barthélémy[3,4] & M. J. Rozenberg[14,15]

As silicon is the basis of conventional electronics, so strontium titanate ($SrTiO_3$) is the foundation of the emerging field of oxide electronics[1,2]. $SrTiO_3$ is the preferred template for the creation of exotic, two-dimensional (2D) phases of electron matter at oxide interfaces[3–5] that have metal–insulator transitions[6,7], superconductivity[8,9] or large negative magnetoresistance[10]. However, the physical nature of the electronic structure underlying these 2D electron gases (2DEGs), which is crucial to understanding their remarkable properties[11,12], remains elusive. Here we show, using angle-resolved photoemission spectroscopy, that there is a highly metallic universal 2DEG at the vacuum-cleaved surface of $SrTiO_3$ (including the non-doped insulating material) independently of bulk carrier densities over more than seven decades. This 2DEG is confined within a region of about five unit cells and has a sheet carrier density of ~0.33 electrons per square lattice parameter. The electronic structure consists of multiple subbands of heavy and light electrons. The similarity of this 2DEG to those reported in $SrTiO_3$-based heterostructures[6,8,13] and field-effect transistors[9,14] suggests that different forms of electron confinement at the surface of $SrTiO_3$ lead to essentially the same 2DEG. Our discovery provides a model system for the study of the electronic structure of 2DEGs in $SrTiO_3$-based devices and a novel means of generating 2DEGs at the surfaces of transition-metal oxides.

In the cubic phase, stoichiometric $SrTiO_3$ has an empty t_{2g} conduction manifold composed of three dispersive, three-dimensional (3D) bands that are degenerate at the Γ point[15]. As schematically shown in Fig. 1a, its band structure along one direction, say k_y, consists of a weakly dispersive (heavy-mass) band and a pair of degenerate, strongly dispersive (light-mass) bands. They arise respectively from the small and large overlaps, along the y axis, of neighbouring titanium $3d_{xz}$, $3d_{xy}$ and $3d_{yz}$ orbitals, as depicted in Fig. 1b for the $3d_{xy}$ orbitals. Thus, the d_{xy}-like band will be light in the x–y plane and heavy along the z axis, whereas the d_{yz} band will be heavy along x and light in the y–z plane, and the d_{xz} band will be heavy along y and light in the x–z plane. The resulting three Fermi surface sheets, projected on the x–y plane of the sample surface, are shown in Fig. 1c for several bulk dopings.

Angle-resolved photoemission spectroscopy (ARPES) is a powerful technique for probing the electronic structure of materials. Previous work using ARPES addressed the bulk electronic structure of doped $SrTiO_3$, revealing dispersing quasiparticle peaks and in-gap features, and discussing possible polaronic effects near the Fermi energy, E_F (refs 16–19). As we shall see, our ARPES data do not conform to the expected lightly doped bulk band picture, but reveal that a novel 2DEG with a complex subband structure, shown schematically in Fig. 1e, is realized at the low-temperature vacuum-cleaved surface of this material.

Crucial to our discoveries is the comparison of samples with very different bulk carrier densities of $n_{3D} < 10^{13}$ cm^{-3} (essentially non-doped), $n_{3D} \approx 10^{18}$ cm^{-3} (low doping) and $n_{3D} \approx 10^{20}$ cm^{-3} (high doping), determined by bulk-sensitive techniques (Supplementary Information, section II). The large difference in doping is apparent even by inspection of the samples (Fig. 2a–c): whereas the non-doped sample is transparent, the highly doped sample is black and shiny.

Our first observation (Fig. 2d) is that even for the transparent, non-doped sample (Fig. 2a), for which no bulk bands at E_F are expected, the cleaved surface yields intense, strongly dispersive bands across the Fermi level. They correspond to a large density of mobile carriers (see below), ensuring that, despite the electron emission, there is no charging of the surface of this otherwise highly insulating sample in the bulk. Equally notable is the fact (Fig. 2d–f) that for all the bulk dopings studied, the electronic states around E_F, and in particular the bandwidths (E_F minus the band bottom) and Fermi momenta, k_F, of the observed bands, are essentially identical. All these observations contrast sharply with the large differences that would be expected from electron-doping in the bulk (Fig. 1c), where the 3D density of carriers scales as k_F^3. The immediate conclusion is that the observed bands correspond to 2D states (see also Supplementary Information, section III).

The spectra in Fig. 2d–f, measured around Γ_{102} and Γ_{012} (points such as B in Fig. 2j), clearly show two strongly dispersing bands, termed upper and lower parabolic bands. In Fig. 2g–i, two other weakly dispersing bands, termed upper and lower shallow bands, are revealed either by rotating the light polarization to be at right angles with respect to the measurement direction, as illustrated for the non-doped sample in Fig. 2g, or by measuring around a Γ point at a larger emission angle in a different Brillouin zone (Γ_{112}, or point C in Fig. 2j), as shown for the low-doped sample in Fig. 2h, i. We note furthermore, from Fig. 2d, g, that the changes in light polarization affect the two strongly dispersing parabolic bands differently, completely suppressing the upper parabolic band in Fig. 2g, whereas the increase in emission angle (compare Fig. 2e with Fig. 2h, i) enhances in the same asymmetric way the negative-k intensities of the two shallow bands and weakens the parabolic bands. These dichroic effects, which are due to dipole transition selection rules[17], unambiguously show that the two parabolic bands have different symmetries, which are also different from a third symmetry common to the two shallow subbands (see also Supplementary Information, section IV). This means that the observed 2D bands are organized by their orbital symmetries.

Figure 3 illustrates the complete set of four bands (dashed lines) overlaid on the data, with the colours of the traced bands representing

[1]CSNSM, CNRS/IN2P3 and Université Paris-Sud, Bâtiments 104 et 108, 91405 Orsay cedex, France. [2]Laboratoire Physique et Etude des Matériaux, UMR 8213 ESPCI-CNRS-UPMC, 10 rue Vauquelin, 75231 Paris cedex 5, France. [3]Unité Mixte de Physique CNRS/Thales, 1 Avenue A. Fresnel, Campus de l'Ecole Polytechnique, 91767 Palaiseau, France. [4]Université Paris-Sud, 91405 Orsay, France. [5]Universität Würzburg, Experimentelle Physik VII, 97074 Würzburg, Germany. [6]Ames Laboratory and Department of Physics and Astronomy, Iowa State University, Ames, Iowa 50011, USA. [7]Laboratoire Léon Brillouin, CEA-CNRS, CEA-Saclay, 91191 Gif-sur-Yvette, France. [8]Gerencia de Investigación y Aplicaciones, Comisión Nacional de Energía Atómica, Avenida General Paz y Constituyentes, 1650 San Martín, Argentina. [9]Instituto Sábato, Universidad Nacional de San Martín – CNEA, 1650 San Martín, Argentina. [10]Institute of Physics and National Laboratory for Condensed Matter Physics, Chinese Academy of Sciences, Zhongguancun nansanjie 8, Beijing 100190, China. [11]Synchrotron SOLEIL, CNRS-CEA, L'Orme des Merisiers, Saint-Aubin-BP48, 91192 Gif-sur-Yvette, France. [12]Institut de Ciència de Materials de Barcelona, ICMAB-CSIC, Campus de la UAB, 08193 Bellaterra, Catalonia, Spain. [13]Institut d'Electronique Fondamentale, Université Paris-Sud, Bâtiment 220, 91405 Orsay, France. [14]Laboratoire de Physique des Solides, Université Paris-Sud, Bâtiment 510, 91405 Orsay, France. [15]Departamento de Física, FCEN-UBA, Ciudad Universitaria, Pabellón 1, Buenos Aires (1428), Argentina.

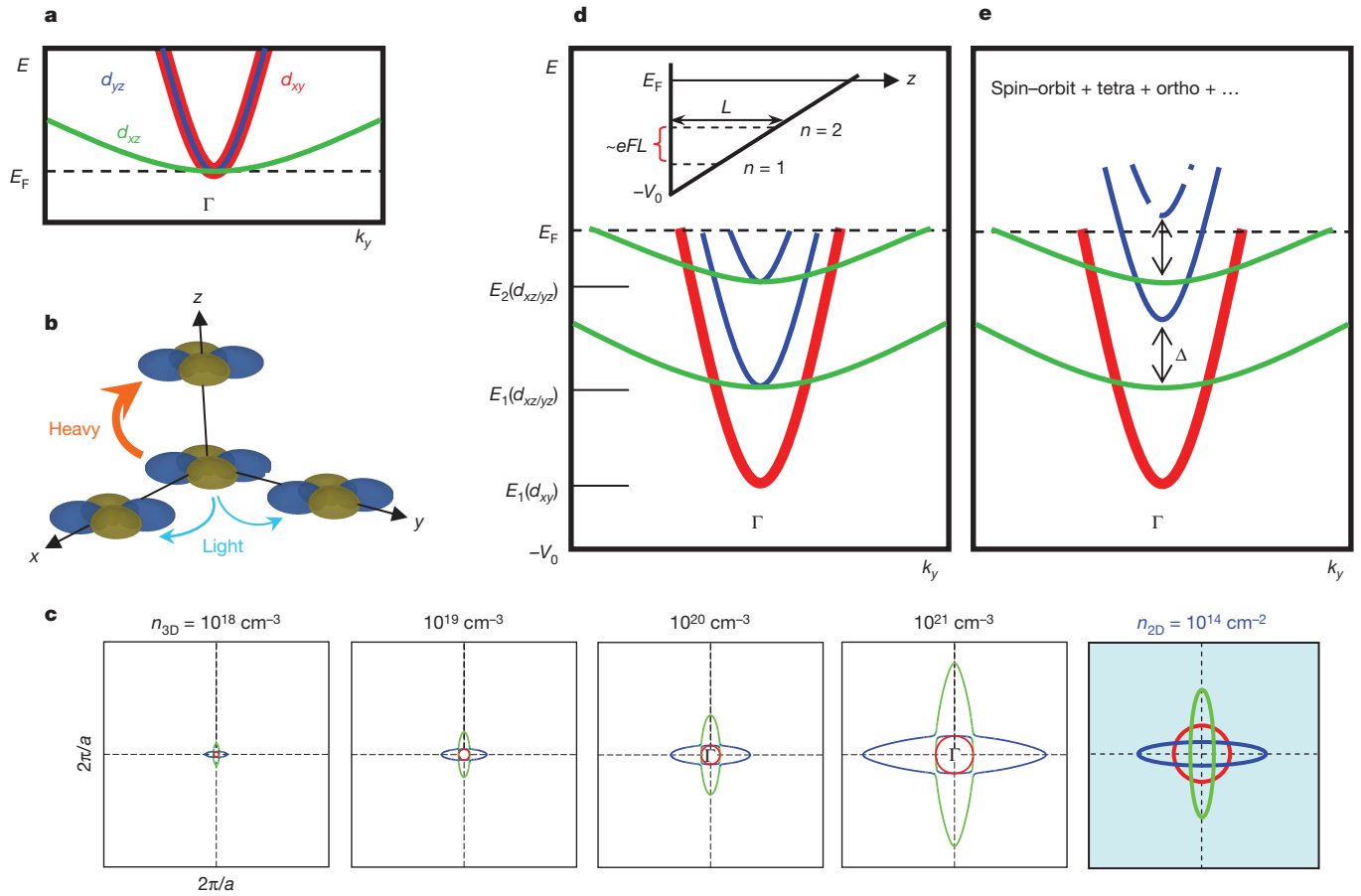

Figure 1 | Electronic structure of $SrTiO_3$ and effects of electron confinement. **a**, Bulk conduction band of $SrTiO_3$ along k_y, consisting of a heavy d_{xz} band (green) and a doublet of light d_{xy}/d_{yz} bands (red and blue). **b**, The bands in **a** stem from the small and large overlaps of the titanium 3*d* orbitals along the *y* direction, depicted here for the case of $3d_{xy}$ orbitals. **c**, Resulting 3D Fermi surfaces (cut along the *x*–*y* plane) for several bulk dopings. The last panel shows, for comparison, the 2D Fermi surface for a 2DEG of density $\sim 10^{14}$ cm^{-2} (hybridization between different Fermi surface sheets is not included), deduced from a tight-binding model[12]. Colours indicate the character of each Fermi surface sheet along k_y. **d**, Quantum well states, or subbands, resulting from the confinement of electrons near the surface of $SrTiO_3$. The inset shows a wedge-like potential created by an electric field of strength *F* at the surface, which we use as a simple model to analyse the ARPES data (see main text). The size, *L*, of the confined 2DEG can be estimated from the extension of the highest occupied state ($n = 2$ in our case) or approximately from the energy difference between the lowest ($n = 1$) and highest occupied states. **e**, Additional degeneracy lifts at Γ occur as a result of spin–orbit coupling, tetragonal and orthogonal distortions, or possible surface reconstructions. This subband hierarchy is the one that best represents the experimental results.

their symmetry characters, discussed further below. We note that this band structure agrees with the one depicted in Fig. 1e.

We now quantitatively analyse the observed band structure. The upper and lower parabolic bands have bandwidths of 210 and 100 meV and Fermi momenta of 0.21 and 0.13 Å^{-1} (best seen in Fig. 3), respectively. Thus, they correspond to light carriers with effective masses $m_y^* \approx 0.7m_e$ along k_y (m_e is the free electron mass). The upper shallow band (Figs 2g, h and 3) has a bandwidth of 40 meV and a Fermi momentum of $k_F \approx 0.3$–0.4 Å^{-1}, corresponding to heavy carriers with $m_y^* \approx 10m_e$–$20m_e$. The lower shallow band (Figs 2i and 3) disperses from about −160 meV at Γ to about −120 meV at the Brillouin zone boundary, and is thus fully occupied. All the above figures differ by less than 10% across all the studied dopings.

As shown in Fig. 4, the resulting Fermi surface consists of a circle of radius 0.21 Å^{-1} and two ellipsoids, along k_x and k_y, with semi-axes of 0.13 and 0.3–0.4 Å^{-1}, respectively. From the area, A_F, enclosed by each Fermi surface, the corresponding 2D carrier density is $n_{2D} = A_F/2\pi^2$. Accounting for the three bands that cross E_F, we find 0.33 ± 0.03 electrons per a^2 (or about 2×10^{14} cm^{-2}), where *a* is the cubic lattice parameter.

We now rationalize the observed electronic states as the subbands of a 2DEG confined within a few unit cells at the surface of $SrTiO_3$. To this end, we consider a potential, V_0, at the surface that confines the electronic motion along *z* (Fig. 1d, inset). This lowers the energy of the bands by about V_0, similar to the 'band bending' in semiconductor heterostructures, and produces an energy splitting between the different eigenstates that is inversely proportional to their effective masses along *z* (m_z*). The resulting subband structure, depicted in Fig. 1d, consists on a single d_{xy}-like band and two d_{xz}/d_{yz} bands that are degenerate at Γ. As the d_{xy} band has a very large m_z*, the attractive confining potential will merely pull it below E_F (its energy-split eigenstates will have a negligible separation). Thus, we identify this band with the lower parabolic band in our spectra of Fig. 2, and denote it $E_1(d_{xy})$. By contrast, the d_{xz} and d_{yz} subbands, which are light along *z*, will show large energy splittings. They are noted $E_n(d_{xz/yz})$ ($n = 1, 2, \ldots$) in Fig. 1d.

Other effects beyond this simplified analysis, such as spin–orbit coupling (which has been reported at the $LaAlO_3/SrTiO_3$ interface[20]) and/or the low-temperature tetragonal and possibly orthorhombic distortions[21,22], can lift the degeneracy between the d_{xz} and d_{yz} subbands, as illustrated in Fig. 1e. This would induce a coupling, resulting in hybridization between the light and heavy subbands, as indeed evidenced by our data for the lower parabolic band and the shallow bands (Fig. 3, linear vertical polarization). Another possibility would be a surface reconstruction, although this is not suggested by our data, which follows the periodicity of the unreconstructed bulk lattice without apparent

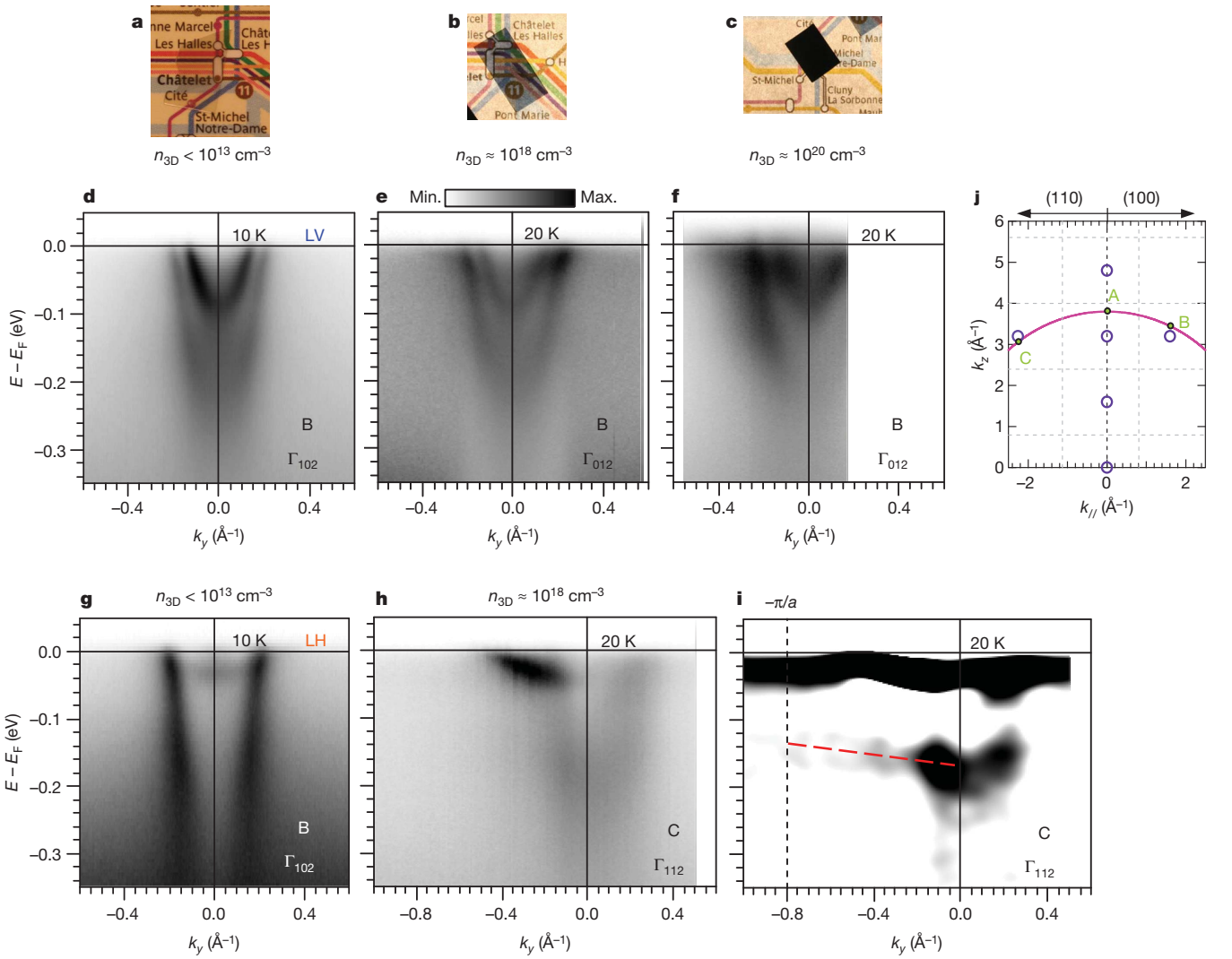

Figure 2 | Universal electronic structure at the surface of $SrTiO_3$. **a**–**c**, Photographs and bulk dopings of the samples studied using ARPES. **d**–**f**, Corresponding energy–momentum intensity maps close to the Γ point (B-like points in **j**). In **d**–**f**, only the upper and lower parabolic bands are best observed, owing to dipole selection rules for the photon polarizations and measurement geometries used (Methods and Supplementary Information, section IV). If the photon polarization is rotated from linear vertical (LV; **d**) to linear horizontal (LH; **g**), the upper shallow band appears and the upper parabolic band disappears, as illustrated here for the non-doped sample. The effects of collecting electrons around a Γ point at a larger emission angle in a different Brillouin zone (point C in **j**) are also shown, for the low-doped sample, in the energy–momentum intensity map in **h** and in the map of the second derivative of this intensity (only negative values shown) in **i**, where the dispersion of the lower shallow band is indicated by a dashed red line. Here the negative-k intensities of the shallow bands are enhanced whereas the intensities of the parabolic bands decrease. **j**, 2D representation of the 3D Brillouin zones of $SrTiO_3$ (dashed lines) in relation to the hemispherical measurement surface in momentum space at an energy of $h\nu = 47$ eV (refs 17, 18). The measurement temperature (10 K or 20 K) is indicated in each panel.

band folding. Resolving the detailed origin of such a degeneracy lift, which is not relevant to the discoveries reported here, will require future investigations. Hence, we identify the lower shallow band and the upper parabolic band in our spectra (Fig. 2) with the components of the split doublet $E_1(d_{xz})$ and $E_1(d_{yz})$, respectively. From the data, the doublet splitting is $\Delta \approx 60$ meV. We finally identify the upper shallow band with $E_2(d_{xz})$. Given that the bottom of this band is at -40 meV, its upper partner, $E_2(d_{yz})$, would occur at about $+20$ meV and cannot be observed.

This subband hierarchy respects the symmetry considerations previously deduced from the effects of light polarization and emission angle, rendering additional support to the picture of a confined 2DEG.

To characterize this 2DEG quantitatively, we use a simple schematic model. We assume that the surface has a homogeneous, positive charge density, generating a confining electric field, F, inside the solid and, thus, a triangular wedge potential of depth V_0 at the surface ($z = 0$) and value $V(z) = -V_0 + eFz$ (e, elementary charge) along z, as depicted in the inset of Fig. 1d. The details of the calculations are presented in Supplementary Information (section VI). From the experimental splitting, $E_2(d_{xz}) - E_1(d_{xz}) = 120$ meV, between the first two subbands of the d_{xz} orbitals, and their light mass, $m_z^* \approx 0.7m_e$, along z, we deduce a strong confining field $F \approx 83$ MV m^{-1}. From $E_1(d_{xy})$, the confining potential is estimated to be $V_0 \approx -260$ meV. The deduced values of V_0 and F, and the measured effective masses and doublet splitting of 60 meV between the d_{xz} and d_{yz} subbands, suffice for the calculation of all the observed subband energies. The width, L, of the confined 2DEG results from the spatial extension of the highest occupied state, $E_2(d_{xz})$, or, independently, from the approximate expression $eFL \approx E_2(d_{xz}) - E_1(d_{xz})$ (Fig. 1d, inset), yielding consistent values in the range $L \approx 14.5$–18 Å, or ~4–5 unit cells. Additionally, from the confining field, F, and the polarizability of the medium, we calculate an induced surface charge density of ~0.25 electrons per a^2, consistent with the experimental value.

The band bending due to confinement should induce an energy downshift of the oxygen $2p$ valence band of about V_0, creating a gap with respect to E_F that is larger than the optical gap. This effect,

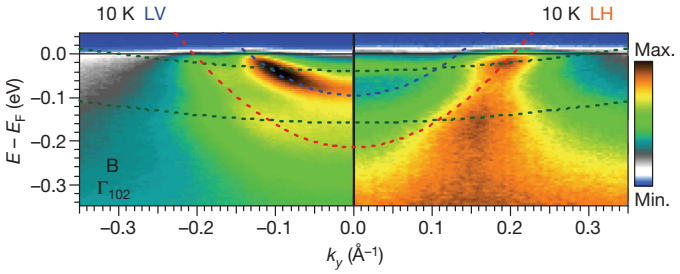

Figure 3 | Summary of subbands for the 2DEG at the surface of $SrTiO_3$. Side-by-side representation of the LV and LH spectra around Γ_{102} for the non-doped sample. An elongated aspect ratio has been used to discern the shallow bands better. The dotted lines are tight-binding representations of the bands[12], following the same colour scheme as in Fig. 1e. Hybridizations between the lower parabolic band and the shallow bands are observed on the spectra taken with LV polarization.

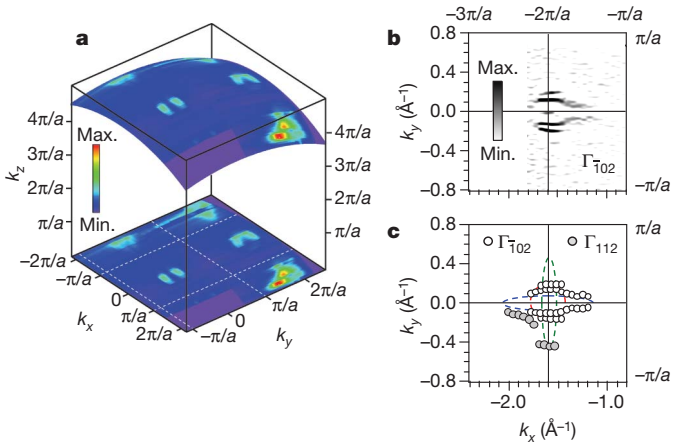

Figure 4 | Fermi surface of 2DEG at the surface of $SrTiO_3$. **a**, ARPES Fermi surface map (integrated within ± 20 meV around E_F) across several Brillouin zones. The map is displayed on the spherical shell of 3D k space corresponding to the measurement photon energy $h\nu = 47$ eV (Methods), and is also projected on the k_x–k_y plane. Owing to dipole selection rules for the measurement geometry used (Supplementary Information, section IV), Fermi surface sheets of different orbital characters are more intense in different Brillouin zones. Thus, the Fermi surface circle from the lower (d_{xy}-like) light parabolic band is best observed in the Γ_{002} and Γ_{012} (and equivalent) Brillouin zones, whereas the two elliptical, perpendicular Fermi surfaces from the upper parabolic band (d_{yz}) and the upper shallow band (d_{xz}) are best observed in off-normal emission (Γ_{012}, Γ_{112} and equivalent). **b**, Second derivative (negative values only) of the Fermi surface map over $\Gamma_{\bar{1}02}$, showing portions of the circular and the elliptical–horizontal Fermi surfaces. The intensity of the vertical ellipse is very weak here owing to dipole selection rules. **c**, Collected Fermi momenta from high-statistics measurements around $\Gamma_{\bar{1}02}$ (white circles) and Γ_{112} (grey circles), and comparison with the Fermi surfaces resulting from the tight-binding bands of Fig. 3 (colours indicate the character along k_y and follow the scheme used in Fig. 1c–e). All panels correspond to measurements on the low-doped sample.

observed in our data (Supplementary Information, section V), was previously reported and studied in ref. 17, where it was demonstrated that when the cleaved surface of $SrTiO_3$ is exposed to oxygen, the oxygen 2p valence band shifts by about 200 meV towards E_F and the quasiparticle peak at E_F, which corresponds to our 2DEG, disappears. Surface oxygen vacancies therefore seem to be the most reasonable candidates to explain the origin of the 2DEG observed in our experiments. In fact, cleaving (or fracturing) is likely to produce a massive removal of surface oxygen, much larger than and basically independent of the bulk concentration of vacancies, providing two dopant electrons per created vacancy. These two electrons will delocalize within the potential wedge created by the positively charged layer of surface vacancies. We note that fracturing this almost cubic oxide system necessitates overcoming the strong binding electric forces between atoms, which is equivalent to inducing a 'mechanical dielectric breakdown'. According to our data analysis, the large electric field generated at the surface of $SrTiO_3$ is of the order of typical dielectric breakdown fields[23], and is thus compatible with a cleaved surface in this material.

To give additional support to our picture and data analyses, we performed *ab initio* calculations including oxygen vacancies at the surface. The results, presented in the Supplementary Information (section VII), are consistent with the above simplified wedge-potential model for the two types (TiO_2 and SrO) of possible surface termination.

Strikingly, the sheet carrier density, the confinement size, the confining field, F, and potential, V_0, and the presence of both mobile and quasi-localized carriers in this novel electron gas at the surface of $SrTiO_3$ compare well with the characteristics of other 2DEGs at different types of $SrTiO_3$ interface[6,8,9,12,13,24–27]. Furthermore, our experiments directly show the emergence, at the surface of $SrTiO_3$, of a metallic subband structure where the titanium $3d_{xy}$ states of light carriers become the first available levels. This situation is similar to that reported in $LaAlO_3/SrTiO_3$ interfaces[28]. These remarkable consistencies suggest that all these 2DEGs may be understood on a common basis. In particular, we note that fundamentally different electron confinement mechanisms, such as the electric field created by a polar $LaAlO_3$ layer[6], the direct application of an electric field[9] or the charge leakage between a Mott insulator and a band insulator[11], would recreate a 2DEG confined within a nanometric layer of $SrTiO_3$ with a subband electronic structure similar in nature to that revealed by our measurements.

Our discoveries demonstrate that a highly mobile 2DEG can be readily obtained without any elaborate interface preparation at the surface of $SrTiO_3$, even in the case of the non-doped 3 eV bandgap insulator. This 2DEG is thus decoupled from the sea of bulk electrons, and constitutes a model system for fundamental and applied research in oxide surfaces/interfaces. An exciting perspective is that other hard-to-cleave complex oxides with multifunctional behaviour, such as multiferroics, ferroelectrics or manganites, might realize similar 2DEGs that inherit the functionalities of the bulk material. Candidates to study in this regard would be other titanates, such as the ferroelectric $BaTiO_3$ or the Mott–Hubbard insulator $LaTiO_3$. The properties of such 2DEGs might be tailored by surface doping with either electron-donor or -acceptor species, something that is not always feasible in the bulk, opening a window to explore new phenomena. This simple approach has been applied successfully to tune the density of states in, for example, the surface states of topological insulators[29]. Our discoveries also raise the appealing possibility that oxygen vacancies may be induced to aggregate or self-organize at the surfaces or interfaces of $SrTiO_3$ or other oxides—a situation that might be at the origin of the reversible patterning of conducting nano-lines in $LaAlO_3/SrTiO_3$[2,7,30]. More generally, we suggest that the nano-engineering of atomic vacancies at the surfaces of transition-metal oxides could provide model systems for low-dimensional, confined electron gases, opening a new avenue in correlated-electron surface science.

METHODS SUMMARY

High-quality, single crystals of $SrTiO_3$ doped with oxygen vacancies (except for the non-doped sample) were measured throughout this work. The ARPES experiments were done at the Synchrotron Radiation Center (University of Wisconsin-Madison) and at the Synchrotron SOLEIL (France), using different photon energies, intensities, polarizations and measurement geometries. In all cases, the angular and energy resolutions were 0.25° and 20 meV, respectively. The samples were fractured *in situ* along the c axis below 20 K at a pressure lower than 6×10^{-11} torr. Using calibrated photodiodes, we checked that the beam intensity per unit area at the same photon energy differs by at least one decade between the two synchrotrons. As the observed 2DEG is identical in both cases, this indicates that its subbands are not significantly populated by photo-carrier injection. The results have been reproduced in at least two samples for each bulk doping. The methods associated with this work are detailed in Methods and Supplementary Information.

Full Methods and any associated references are available in the online version of the paper at www.nature.com/nature.

Received 23 July; accepted 26 November 2010.

1. Ramirez, A. P. Oxide electronics emerge. *Science* **315,** 1377–1378 (2007).
2. Cen, C., Thiel, S., Mannhart, J. & Levy, J. Oxide nanoelectronics on demand. *Science* **323,** 1026–1030 (2009).
3. Ohtomo, A. & Hwang, H. Y. A high-mobility electron gas at the $LaAlO_3/SrTiO_3$ heterointerface. *Nature* **427,** 423–426 (2004).
4. Ahn, C. H., Triscone, J.-M. & Mannhart, J. Electric field effect in correlated oxide systems. *Nature* **424,** 1015–1018 (2003).
5. Ohtomo, A., Muller, D. A., Grazul, J. L. & Hwang, H. Y. Artificial charge-modulation in atomic-scale perovskite titanate superlattices. *Nature* **419,** 378–380 (2002).
6. Thiel, S., Hammer, G., Schmehl, A., Schneider, C. W. & Mannhart, J. Tunable quasi-two-dimensional electron gases in oxide heterostructures. *Science* **313,** 1942–1945 (2006).
7. Cen, C. *et al.* Nanoscale control of an interfacial metal–insulator transition at room temperature. *Nature Mater.* **7,** 298–302 (2008).
8. Reyren, N. *et al.* Superconducting interfaces between insulating oxides. *Science* **317,** 1196–1199 (2006).
9. Ueno, K. *et al.* Electric-field-induced superconductivity in an insulator. *Nature Mater.* **7,** 855–858 (2008).
10. Brinkman, A. *et al.* Magnetic effects at the interface between non-magnetic oxides. *Nature Mater.* **6,** 493–496 (2007).
11. Okamoto, S. & Millis, A. J. Electronic reconstruction at an interface between a Mott insulator and a band insulator. *Nature* **428,** 630–633 (2004).
12. Popović, Z. S., Satpathy, S. & Martin, R. M. Origin of the two-dimensional electron gas carrier density at the $LaAlO_3$ on $SrTiO_3$ interface. *Phys. Rev. Lett.* **101,** 256801 (2008).
13. Basletic, M. *et al.* Mapping the spatial distribution of charge carriers in $LaAlO_3/SrTiO_3$ heterostructures. *Nature Mater.* **7,** 621–625 (2008).
14. Nakamura, H. *et al.* Tuning of metal-insulator transition of two-dimensional electrons at parylene/$SrTiO_3$ interface by electric field. *J. Phys. Soc. Jpn* **78,** 083713 (2009).
15. Mattheiss, L. F. Energy bands for $KNiF_3$, $SrTiO_3$, $KMoO_3$ and $KTaO_3$. *Phys. Rev. B* **6,** 4718–4740 (1972).
16. Fujimori, A. *et al.* Doping-induced changes in the electronic structure of $La_xSr_{1-x}TiO_3$: limitation of the one-electron rigid-band model and the Hubbard model. *Phys. Rev. B* **46,** 9841–9844 (1992).
17. Aiura, Y. *et al.* Photoemission study of the metallic state of lightly electron-doped $SrTiO_3$. *Surf. Sci.* **515,** 61–74 (2002).
18. Ishida, Y. *et al.* Coherent and incoherent excitations of electron-doped $SrTiO_3$. *Phys. Rev. Lett.* **100,** 056401 (2008).
19. Chang, Y. J., Bostwick, A., Kim, Y. S., Horn, K. & Rotenberg, E. Structure and correlation effects in semiconducting $SrTiO_3$. *Phys. Rev. B* **81,** 235109 (2010).
20. Caviglia, A. D. *et al.* Tunable Rashba spin-orbit interaction at oxide interfaces. *Phys. Rev. Lett.* **104,** 126803 (2010).
21. Lytle, F. W. X-ray diffractometry of low-temperature phase transformations in strontium titanate. *J. Appl. Phys.* **35,** 2212–2215 (1964).
22. Mattheiss, L. F. Effect of the 110°K transition on the $SrTiO_3$ conduction bands. *Phys. Rev. B* **6,** 4740–4753 (1972).
23. Barret, H. H. Dielectric breakdown of single-crystal strontium titanate. *J. Appl. Phys.* **35,** 1420–1425 (1964).
24. Copie, O. *et al.* Towards two-dimensional metallic behavior at $LaAlO_3/SrTiO_3$ interfaces. *Phys. Rev. Lett.* **102,** 216804 (2009).
25. Seo, S. S. A. *et al.* Multiple conducting carriers generated in $LaAlO_3/SrTiO_3$ heterostructures. *Appl. Phys. Lett.* **95,** 082107–082109 (2009).
26. Sing, M. *et al.* Profiling the interface electron gas of $LaAlO_3/SrTiO_3$ heterostructures with hard X-ray photoelectron spectroscopy. *Phys. Rev. Lett.* **102,** 176805 (2009).
27. Pentcheva, R. & Pickett, W. E. Ionic relaxation contribution to the electronic reconstruction at the n-type $LaAlO_3/SrTiO_3$ interface. *Phys. Rev. B* **78,** 205106 (2008).
28. Salluzzo, M. *et al.* Orbital reconstruction and the two-dimensional electron gas at the $LaAlO_3/SrTiO_3$ interface. *Phys. Rev. Lett.* **102,** 166804 (2009).
29. Hsieh, D. *et al.* A tunable topological insulator in the spin helical Dirac transport regime. *Nature* **460,** 1101–1105 (2009).
30. Xie, Y., Bell, C., Yajima, T., Hikita, Y. & Hwang, H. Y. Charge writing at the $LaAlO_3/SrTiO_3$ surface. *Nano Lett.* **10,** 25882591 (2010).

Supplementary Information is linked to the online version of the paper at www.nature.com/nature.

Acknowledgements We are grateful to N. Bontemps, R. Claessen, Y. Fagot-Revurat, M. Gabay, I. C. Infante, D. Malterre, A. J. Millis and F. Reinert for discussions, to E. Jacquet for help with the sample preparation and to R. Guerrero for help with the transport measurements. This work was supported by the ANR OXITRONICS and the CNRS-CSIC PICS 'POSTIT' project under grant number PICS2008FR1. The Synchrotron Radiation Center, University of Wisconsin-Madison, is supported by the National Science Foundation under award no. DMR-0537588. The Ames Laboratory is operated for the US DOE by Iowa State University under contract number W-7405-ENG-82. R.W. is a research fellow of CONICET-Argentina, supported by CONICET (grant PIP 112-200801-00047) and ANPCyT grant PICT 837/07. X.G.Q. is supported by the MOST and NSF of China, and G.H. is supported by the Spanish Government under project numbers MAT2008-06761-C03 and NANOSELECT CSD2007-00041.

Author Contributions A.F.S.-S. and O.C. contributed equally to this work, from project conception and ARPES measurements to data analysis, interpretation and writing of the manuscript. The contributions of other authors are as follows. Project conception: G.H., M.B., A.B., M.J.R.; ARPES measurements: T.K., F.F., S.P., F.B., A.N.; infrastructure for ARPES experiments at SOLEIL: F.B., A.T.-I., P.L.F.; samples: X.G.Q., G.H., M.B., Y.A., P.L., A.B.; transport measurements: N.R., Y.A.; data analysis, interpretation, slab-LDA calculations: R.W., M.J.R.; input to writing the manuscript: M.J.R. All authors extensively discussed the results and the manuscript.

Author Information Reprints and permissions information is available at www.nature.com/reprints. The authors declare no competing financial interests. Readers are welcome to comment on the online version of this article at www.nature.com/nature. Correspondence and requests for materials should be addressed to A.F.S.-S. (andres.santander@csnsm.in2p3.fr).

METHODS

Sample preparation and measurement technique. High-quality, single crystals of $SrTiO_3$ were doped with oxygen vacancies by high temperature treatment in low oxygen pressure, except for the non-doped sample, which was a bare $SrTiO_3$ substrate measured without any previous preparation. The bulk carrier concentrations were deduced from Hall and resistivity measurements (Supplementary Information, section II).

The ARPES experiments were done at the Synchrotron Radiation Center (SRC, University of Wisconsin-Madison) and at the Synchrotron SOLEIL (France), using 47 eV (SRC) and 45 eV (SOLEIL) linearly polarized photons, a Scienta 2002 detector with horizontal slits for the highly doped sample (SRC), and a Scienta R4000 with vertical slits for the low-doped (SRC) and non-doped (SOLEIL) samples. The above photon energies, close to resonant photoemission at the titanium 3*p*–3*d* edge, yield intense quasiparticle peaks in $SrTiO_3$ (ref. 17). The momentum and energy resolutions were 0.25° and 20 meV, respectively. The mean diameter of the incident photon beam was less than 50 μm at the Synchrotron SOLEIL and about 300 μm at the SRC. We checked, using calibrated photodiodes, that the photon beam intensity per unit area at the above photon energies differs by at least one order of magnitude between SOLEIL and the SRC. As the observed subbands are the same in both cases, this indicates that the 2DEG is the intrinsic stable state of the ultrahigh-vacuum fractured surface of $SrTiO_3$, and that its subbands are not significantly populated by photo-carrier injection.

The samples were fractured *in situ* along the *c* axis at 20 K (SRC) or 10 K (SOLEIL), at a pressure lower than 6×10^{-11} torr. After fracturing, one narrow, highly emitting region was selected and kept fixed for each set of measurements. Supplementary Information (section I) presents details of the fracturing procedure and a discussion of the surface terminations in relation to the data shown here.

The Fermi momenta and bandwidths were determined from the peak positions of the momentum distribution curves at $E = 0$ and the energy distribution curves at $k = 0$, respectively.

The results have been reproduced in at least two samples for each bulk doping.

Measurement geometries. The sample's surface defines the *x*–*y* plane. The crystals were oriented using Laue diffraction and mounted with the (010) axis along the angle-resolved direction of the detector, defining the k_y direction. The photon energy fixes the radius of the *k*-space hemisphere for the measurements, which was $\sim 3.8\,\text{Å}^{-1}$ (or about $0.7\pi/a$ above Γ_{002}) for $SrTiO_3$ at photon energies around 47 eV (refs 17, 18). The data in Figs 2d, g and 3 were collected from B-like points slightly above Γ_{102}, with the photon polarization along *y* (LV) in Fig. 2d and in the *x*–*z* plane (LH) in Fig. 2h. The data in Figs 2e, f correspond to B-like points slightly above Γ_{012} and those in Figs 2h, i correspond to C-like points slightly below Γ_{112}. For these points, the photon polarization is not parallel to any of the sample's symmetry directions or planes, and the spectra have different symmetry mixtures. The data in Fig. 4 were collected with LH photon polarization. Supplementary Information (section IV) discusses further the measurement geometries and their corresponding dipole selection rules.